TESS observations of flares and quasi-periodic pulsations from low mass stars and potential impact on exoplanets

Gavin Ramsay[1] · Dmitrii Kolotkov[2,3] · J.Gerry Doyle[1] · Lauren Doyle[4,5]

Abstract We have performed a search for flares and Quasi-Periodic Pulsations (QPPs) from low mass M dwarf stars using TESS 2 min cadence data. We find seven stars which show evidence of QPPs. Using Fourier and Empirical Mode Decomposition techniques, we confirm the presence of 11 QPPs in these seven stars with a period between 10.2 and 71.9 min, including an oscillation with strong drift in the period and a double-mode oscillation. The fraction of flares we examined which showed QPPs (7 percent) is higher than other studies of stellar flares, but is very similar to the fraction of Solar C-class flares. Based on the stellar parameters taken from the TESS Input Catalog, we determine the lengths and magnetic field strengths of the flare coronal loops using the period of the QPPs and various assumptions about the origin of the QPPs. We also use a scaling relationship based on flares from Solar and Solar-type stars and

✉ G. Ramsay
  gavin.ramsay@armagh.ac.uk

  D. Kolotkov
  d.kolotkov.1@warwick.ac.uk

  J.G. Doyle
  gerry.doyle@armagh.ac.uk

  L. Doyle
  lauren.doyle@warwick.ac.uk

[1] Armagh Observatory and Planetarium, College Hill, Armagh, BT61 9DG, N. Ireland, UK

[2] Centre for Fusion, Space and Astrophysics, Department of Physics, University of Warwick, Coventry, CV4 7AL, UK

[3] Institute of Solar-Terrestrial Physics SB RAS, Irkutsk 664033, Russia

[4] Centre for Exoplanets and Habitability, University of Warwick, Coventry, CV4 7AL, UK

[5] Department of Physics, University of Warwick, Coventry, CV4 7AL, UK

arXiv:2108.10670v1 [astro-ph.SR] 24 Aug 2021

the observed energy, plus the duration of the flares, finding that the different approaches predict loop lengths which are consistent to a factor of $\sim$2. We also discuss the flare frequency of the seven stars determining whether this could result in ozone depletion or abiogenesis. Three of our stars have a sufficiently high rate of energetic flares which are likely to cause abiogenesis. However, two of them are also in the range where ozone depletion is likely to occur. We speculate on the implications for surface life on these stars and the effects of the loop lengths and QPPs on potential exoplanets in the habitable zone.

1. Introduction

The Sun's variable magnetic activity influences its surrounding heliosphere which leads to a variety of observed phenomenon from small-scale features such as spicules to large-scale events such as flares, coronal mass ejections; the latter of these leads to space weather which affects Earth. Flares and coronal mass ejections pose a danger to electric power grids and telecommunications facilities, satellites and astronauts, e.g. (National Research Council , 2008). Furthermore, the Sun's radiative output can affect planetary and global climate on much longer timescales from decades to stellar evolutionary timescales, e.g. (Mursula et al. , 2007; Nandy et al. , 2021). However, we now know that the Sun is much less active than most Solar-type stars, although it remains unclear whether the Sun was always less active or whether its activity levels have declined over millions of years, e.g. Reinhold et al. (2020).

Unlike Solar type stars which have a radiative core and a convective envelope, stars with a mass $\lesssim 0.4 M_\odot$ (corresponding to a $\sim$M4V or later spectral type) are fully convective. The fraction of low mass stars which show optical flares increases from M1V ($\sim$5 percent) to M6V ($\sim$45 percent, Günther et al. , 2020) showing low mass stars are active. One of the principal factors in determining the degree of flare activity is a stars age, with activity declining as stars get older, e.g. Skumanich (1986) and more recently by Davenport et al. (2019). Understanding stellar activity in general has become an area of renewed interest for several reasons. Stellar activity can mask or give false positive detections of exoplanets, e.g. Rajpaul et al. (2015) and stellar flares can effect the atmosphere of planets orbiting their host star, e.g. Airapetian et al. (2020). However, in more recent years, it has been argued that the UV flux incident on an exoplanet, which flares can deliver, are essential for life to form, e.g. Rimmer et al. (2018).

In recent years, there has been major advancements in the detection and analysis of quasi-periodic pulsations (QPPs) in Solar and stellar flares. These QPPs can appear at all phases of a flare from the impulsive to decay phase. Based on a number of statistical studies, QPPs are shown to be a frequent and wide-spread phenomena. There are over a dozen possible mechanisms which produce oscillations in a plasma. In flares from M dwarfs, we have seen sub-second pulses in radio bursts (Osten & Bastian , 2006, 2008), a few tens of seconds in ultra-violet data (Doyle et al. , 2018) and tens of minutes in optical data from *Kepler*

(Pugh et al. , 2016). The proposed models include magnetohydrodynamic waves, repetitive reconnection and oscillations in current sheets. It is also possible that different mechanisms operate in different flares. By studying these properties we can gain important insights to the physical nature of flares and their immediate environment. This allows for the development of theoretical models which explain the origin and properties of both Solar and stellar flares.

The first detection of QPPs in stellar flares was from a M4e star which showed oscillations in the optical on a period of around a dozen seconds using photoelectric observations (Rodono , 1974). It was much later that QPPs were also seen in X-ray observations of a stellar flare, this time on a period of a dozen minutes (Mitra-Kraev et al. , 2005). QPPs with timescales shorter than a dozen minutes have now been seen from many stars, see also Balona et al. (2015). In addition to those given by Pugh et al. (2016), an example of a long period QPP was from YZ CMi (M4.5e) which had a period of 32 minutes (Anfinogentov et al. , 2013). Reale et al. (2018) report X-ray observations of 3 hr pulsations in two pre-main sequence stars, implying a very large stellar loop structure. Cho et al. (2016) made a comparison between the observed characteristics of Solar and stellar QPPs seen in X-rays and concluded that the underlying mechanism responsible was the same in both the Solar and stellar atmospheres. For reviews of QPPs from Solar and stellar flares see McLaughlin et al. (2018); Van Doorsselaere et al. (2016); Kupriyanova et al. (2020); Zimovets et al. (2021).

The means of detecting flares from many stars simultaneously has been transformed with the *Kepler* and *TESS* missions. *Kepler* stared at the same 115 square degree field of view for nearly four years resulting in hundreds of flares being observed from stars of different spectral type (e.g. Davenport , 2016). *TESS* has now observed a large fraction of the sky with photometry available for each sector of sky, each lasting approximately a month in duration. Flares have been seen from stars including Solar type stars (e.g. Doyle et al. , 2020; Tu et al. , 2020) and M dwarfs (e.g. Ramsay et al. , 2020; Günther et al. , 2020). Observations of the nearest star to our Sun, Proxima Centauri (M5.5V), made using *TESS*, showed two flares with QPPs on a timescale of a few hrs (Vida et al. , 2019) indicating that *TESS* could open up a large sample of QPP events from low mass stars.

In this paper we use *TESS* data taken with 2 min cadence to search for high amplitude flares from low mass stars. We identify those which have relatively long duration events (a few hrs) and show evidence for QPPs in the decline from maximum. We apply a sophisticated set of tests to determine the significance of the candidate QPPs and then determine the length of the flare loop structures based on the stars radius and mass. We also discuss the effects of the high energy flares on the atmosphere of exoplanets and whether QPPs themselves could make an impact. Finally we draw parallels between stellar and Solar activity.

2. *TESS* observations

TESS was launched in April 2018 and consists of four 10.5 cm telescopes that observe a $24° \times 96°$ strip (known as a *sector*) of sky for $\sim$28 days (see Ricker et

al. , 2015, for details). Between July 2018 and June 2019, *TESS* covered most of the southern ecliptic hemisphere (Cycle 1) and between July 2019 and June 2020 covered most of the northern ecliptic hemisphere (Cycle 2). Although there is a band along the ecliptic plane which was not observed, at the ecliptic poles there is a continuous viewing zone where stars can be observed for ∼1 yr (to avoid stray light from the Earth and Moon some areas of the northern hemisphere were not observed as originally intended). Each 'full-frame image' has an exposure time of 30 min. However, in each sector, photometry with a cadence of 2 min is obtained, with most targets being selected from the community via a call for proposals.

Since our study requires well sampled light curves with enough resolution to resolve QPPs, we have used 2 min cadence data from Cycles 1 and 2. Using the stars observed in each sector, we find that 217,834 unique stars were observed in 2 min cadence in Cycles 1 and 2 which were also in Gaia DR2 (Gaia , 2018). To select low mass stars we cross-matched the sky co-ordinates of our sample with that of Gaia DR2 and obtained the stars $(BP - RP)$ colour. We derived their absolute G mag using the parallax and a Galactic scale length L=1.35 kpc (Astraatmadja & Bailer-Jones , 2016). Following on from Ramsay et al. (2020) we chose to select stars which have a Gaia colour $(BP - RP) > 1.8$ and are close to the main sequence. Our selection excludes stars which are likely to be in binary systems; are likely younger than ∼30 Myr or have significant reddening (which is unlikely for relatively bright nearby M dwarfs): this gave 15,437 unique stars.

We downloaded the calibrated light curves of our targets from the MAST data archive[1]. We initially used the data values for `SAP_FLUX`, which are the Simple Aperture Photometry values derived using the standard pipeline and normalised each light curve to unity on a sector by sector basis. For those stars with data from more than one sector we made one combined light curve.

For each of the 15,437 light curves, we identified those which had at least one point with a maximum of 1.6 times the mean (corresponding to 0.5 mag in amplitude) and was also 5 times the rms of the full light curve. Each light curve which passed this selection procedure was manually inspected to ensure the event was not due to obvious instrumental effects or a minor planet passing over the field, which show a symmetric profile.

A total of 481 stars showed at least one flare with an amplitude of 0.5 mag and also passed our initial manual verification phase. Of this sample, 178 stars had at least one high amplitude flare which had a duration greater than 1 hr, with 40 having a duration of 2 hr or more. The light curve of each of the 178 stars were then visually inspected to search for candidate QPPs in the decline from flare maximum. We identified seven stars which show evidence for candidate QPPs events: three stars showed more than one candidate QPP event in separate flares.

The physical and observational characteristics of these stars are outlined in Table 1. We show in Fig. 1 the position of these stars in the Gaia $(BP - RP)$, M_G plane. This indicates that they have spectral types around M3–M4V[2], the point where stars become fully convective.

---

[1] https://archive.stsci.edu/tess/

[2] https://www.pas.rochester.edu/~emamajek/EEM_dwarf_UBVIJHK_colors_Teff.txt
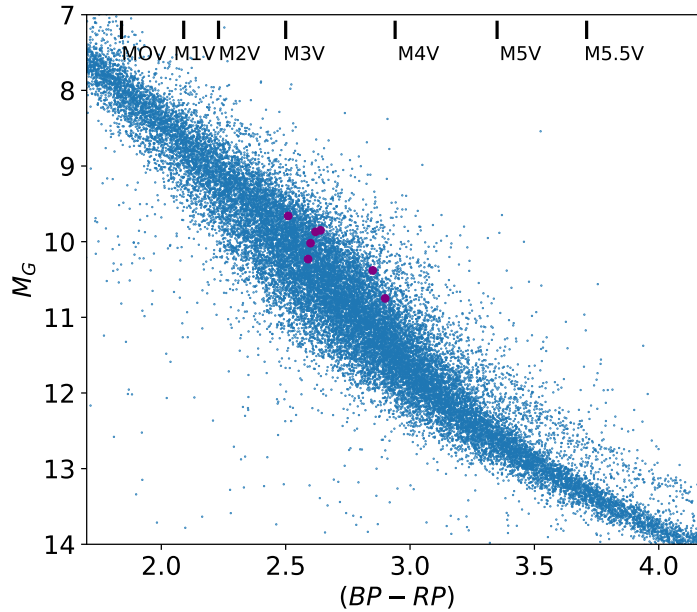
Figure 1. Stars within 50 pc are shown as small blue dots in the Gaia $(BP - RP)$, M_G plane. Purple dots show those stars which we identified as having candidate QPPs in at least one flare event. Using the work of Pecaut & Mamajek (2013), we find they have a spectral type in the range M3–M4V.

We then considered the issue of the large pixel size (21 arcsec per pixel) of the detectors on the *TESS* cameras which can cause variability from spatially nearby stars to contaminate the light curve of the target star. We initially used `tpfplotter` (Aller et al. , 2020) to overlay the position of stars in the Gaia DR2 catalogue onto an image derived from a TESS Target Pixel File (see the lower panel of Fig. 2). This indicates which, if any, stars were in the aperture mask used to extract the light curve of the target, which typically is 7–8 pixels in size. Of the seven stars in our sample, three had no stars within 3 mag of the target in the aperture mask. For the remaining four stars, the stars were between 2.8 – 2.9 mag fainter than the target. Using Gaia EDR3 data to determine their place on the Gaia HRD we identify the spatially nearby stars as being late K or early M spectral types.

The Target Pixel files also allowed us to examine how the position of the center of the photocentre of the Point Spread Function (PSF) ($\texttt{MOM}_{CENTR1/2}$) varied over the observation. It is quite normal for the position of the photocenter to shift by a few 0.01 pixels in x,y co-ordinates over the ~13–14 days which make up half of a sector's observations. What we find is that even for stars which have no spatially nearby stars in the aperture mask, during more intense flares the photocenter can shift by ~0.1 pixels in x,y co-ordinates. As an example, we show

Table 1. The stellar parameters for the sources which we have identified QPPs in at least one flare observed using *TESS* 2 min cadence data. The data has been extracted from the TIC v8.0 (Stassun et al. , 2019) and Gaia DR2.

TICID	Tmag	RA (2000)	DEC (2000)	pmra (mas/yr)	pmdec (mas/yr)	$BP - RP$	D (pc)	MG	L (erg/s)	$T_{\rm eff}$ (K)	Radius ($R_\odot$)	Mass ($M_\odot$)
1403938	13.84	140.26158	-15.89001	-92.3±0.1	30.7±0.1	2.85	83.9±0.8	10.38	5.0E31	3251±157	0.371±0.011	0.358±0.02
233547261	13.24	281.73833	60.89595	14.8±0.1	-26.5±0.1	2.60	78.1±0.4	10.02	6.4E31	3376±157	0.390±0.012	0.381±0.02
279494336	12.9	59.08738	-15.80579	-13.7±0.1	-46.7±0.1	2.62	72.9±0.5	9.87	6.9E31	3366±157	0.407±0.012	0.399±0.02
353898013	12.63	271.89985	56.32422	22.9±0.1	41.2±0.1	2.90	43.9±0.2	10.75	3.8E31	3230±157	0.328±0.010	0.309±0.02
455825451	12.19	322.41897	64.09441	90.9±0.1	28.8±0.1	2.59	43.8±0.1	10.23	5.8E31	3384±157	0.369±0.011	0.356±0.02
271698144	12.63	110.13863	-75.76763	-35.8±0.1	71.4±0.1	2.51	69.6±0.3	9.66	8.3E31	3429±157	0.431±0.013	0.426±0.02
393804343	12.93	81.32051	-20.90736	20.8±0.1	-40.7±0.1	2.64	74.8±0.6	9.85	7.2E31	3361±157	0.418±0.012	0.411±0.02

in the top panel of Fig. 2 the position of the centroid of the photocenter of TIC 271698144 (one of our selected objects) over the course of a high amplitude flare: it shifts in x,y by a few 1/100 of a pixel *towards* the target (although in other cases it was not). We also show a map of the immediate field with the location of the aperture mask shown. The spatially nearby stars are at least 5 mag fainter than the target. The only explanation we can attribute to this observation is chromatic aberration which will be sensitive to position of the target in the plane of the detector. During a high amplitude flare, the colour of the incident light is hotter (bluer) and therefore could in principal be slightly offset from the previous centroid. This has been studied in depth for *Kepler* data by Hedges et al. (2021) who show the shape of the PSF varies depending on the colour and note that due to the refractive nature of the *TESS* optics this effect is likely to be much greater in *TESS* data. Finally, we note that Jackman et al. (2021) made a systematic study of flares from M dwarfs using *Kepler* and *TESS* data and conclude that for *TESS* data there is a 5.8 percent chance of a false positive flare event due to spatially nearby stars. We conclude that it is highly unlikely that the flares in which we detect candidate QPPs do not originate from the M dwarf target.

For each of the seven stars which passed this verification phase we took the bolometric luminosity of our target stars from the TIC V8.0 catalogue (Stassun et al. , 2019). Determining the luminosity of the flares involves some degree of approximation. Unlike the photosphere of the M dwarf star, the temperature of the flare can be considerably higher. We assume that the temperature of the flare is ∼12,000 K and that the fraction of the emitted flux which falls within the *TESS* pass-band is ∼0.14 (Schmitt et al. , 2019). This implies a correction factor of ∼7 to obtain the bolometric luminosity of the flare (this gives flare energies ∼1.5 greater compared with a temperature of 9,000K, (Howard et al. , 2019)). With this in place, we then removed the signature of the rotational modulation and instrumental effects using a routine in the `lightkurve` python package (Lightkurve Collaboration , 2018). We then searched for flares and calculated the energy of *all* the flares in that light curve using the `Altaipony`[3] suite of python based software which is an update of the `Appaloosa` (Davenport

---

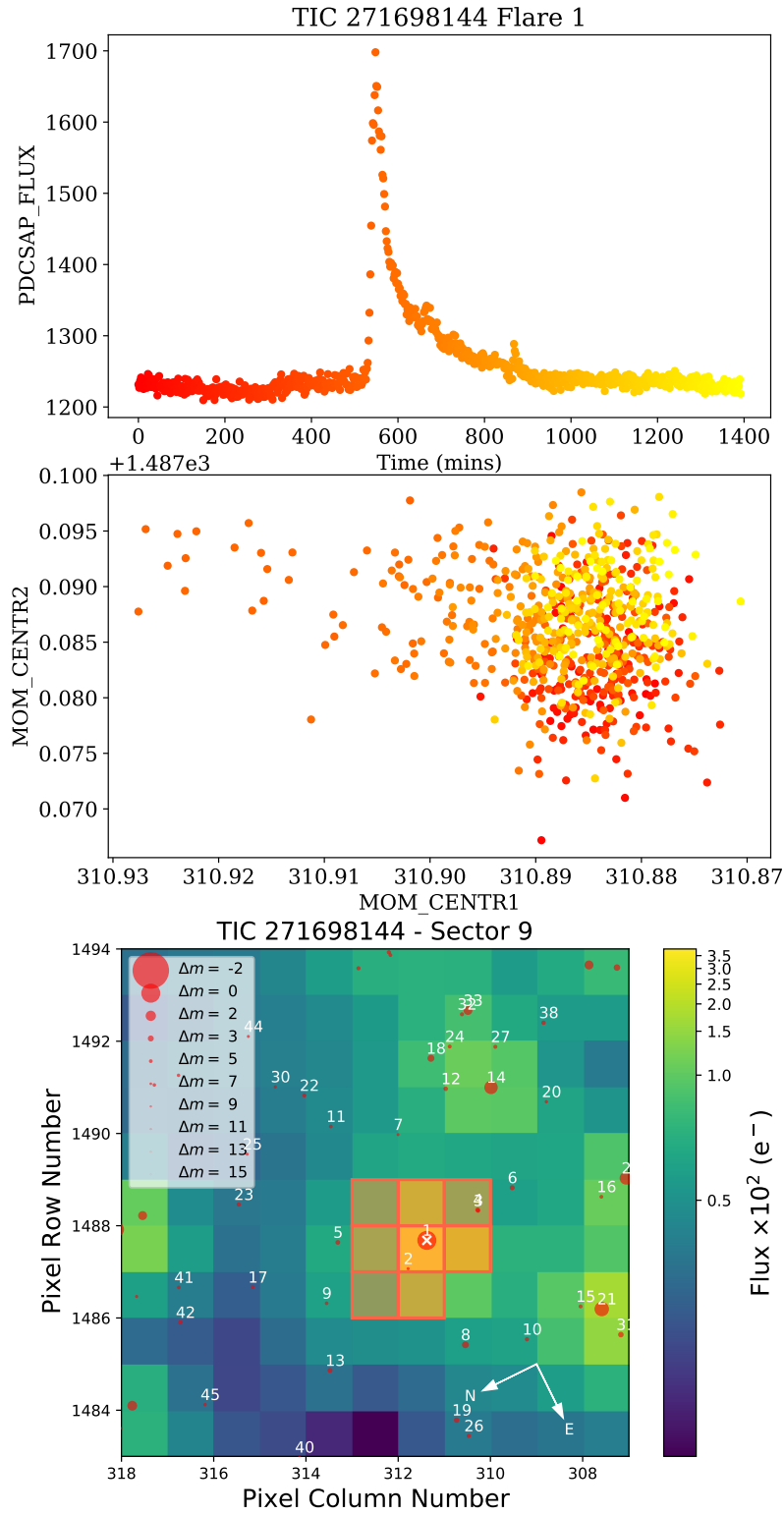[3]https://altaipony.readthedocs.io/en/latest

Figure 2. In the top panel we show the light curve of the first flare we detect in TIC 271698144 colour coded in such a way that it reflects the detector coordinates in the middle panel. Middle panel indicates that during the flare the centroid of the photocenter shifts to the upper left. The lower panel shows a map of the immediate field taken from the Target Pixel File with the aperture map shown as red boxes. The spatially nearby stars are all at least 5 mag fainter than the target. During the flare, the photocenter shifts *towards* the target. We attribute this to chromatic aberration.

Table 2. For those stars showing candidate QPPs, we show the duration of the *TESS* light curve; the period which we take to be the rotation period; the amplitude of the rotation period; the maximum bolometric energy of the flares seen, the total number of flares detected and the number of flares with QPPs.

TIC	Duration (d)	Period (d)	Amp (frac)	Max Energy (erg)	No. Flares	No. Flares with QPPs
1403938	18.6	0.645	0.0104	6.0×10^{35}	2	2
233547261	321.6	2.45	0.0380	2.3×10^{36}	24	1
279494336	46.9	0.924	0.0060	6.1×10^{35}	2	1
353898013	321.5	1.659	0.0294	1.1×10^{36}	79	1
455825451	95.5	0.478	0.0332	7.8×10^{35}	31	1
271698144	287.0	0.419	0.0100	8.1×10^{35}	85	2
393804343	45.2	0.912	0.0202	8.7×10^{35}	17	3

, 2016) suite of software. To determine the likely rotation period of the stars, we used the light curves derived from the `PDCSAP_FLUX` values, which are the Simple Aperture Photometry values, `SAP_FLUX`, after correction for systematic trends and the Lomb Scargle (LS) Periodogram as implemented in the `VARTOOLS` suite of tools (Hartmann & Bakos , 2016). We show the periods of each star in Table 2: where (i) each period was clearly seen in the light curve, (ii) has a very low False Alarm Probability and (iii) is within the range 0.4–2.5 d. We now go on to a detailed assessment of the candidate QPP events, returning to the wider implications of the rate of high energy flares from these stars in §6.

3. Searching for QPPs

We found seven low mass M dwarf stars with candidate QPPs in their *TESS* light curves. How to detect the presence of QPPs in stellar flares and determine their significance is a challenging task with many different approaches having been used over the years. Broomhall et al. (2019) outline the potential pitfalls in these approaches and make a number of recommendations for such searches.

For identifying the flare events to be checked for the presence of QPP patterns in all of the available observations, we begin with assuming $t_{\text{rise}} = 100$ min for pre-flare and flare rising phases and $t_{\text{dec}} = 500$ min for the flare decay phase. For each of the light curves, we set a threshold of 3-σ, where the standard deviation was derived from the full light curve and identify all local maxima exceeding this threshold. From the identified local maxima, we select only those where the time interval is greater than $0.3 t_{\text{dec}}$ (thus we consider the events with multiple maxima situated closer than $0.3 t_{\text{dec}}$ with respect to each other as a single event). The selected maxima preceded by t_{rise} and followed by t_{dec} thus become the list of flaring events for the further QPP analysis (see the red triangles in Figs. 3-4 and Figs. 9-11).
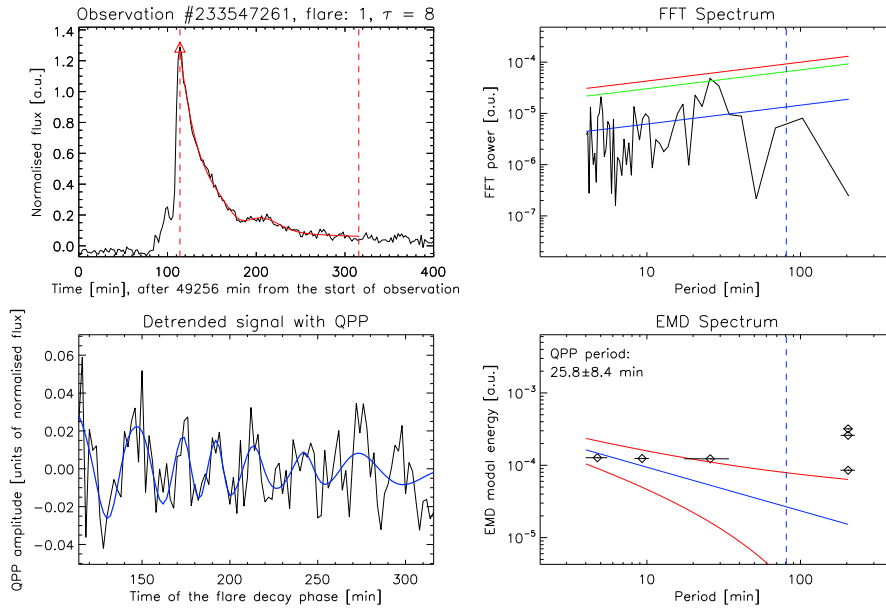
Figure 3. A QPP event manifesting strong drift in the oscillation period. Top left: the flare light curve (the black line) and a low-frequency trend $T(t)$ of its decay phase (the red line), obtained as described in Sec. 3, step 7. The vertical dashed lines indicate the time interval of interest. The red triangle shows the position of the apparent flare peak (the highest value in the light curve). Bottom left: The original flare section of interest with the low-frequency trend subtracted (the black line). The blue line shows the EMD-revealed statistically significant intrinsic mode. Top right: the Fourier power spectrum of the detrended flare signal shown in the bottom left panel in black. The blue solid line shows the best-fit of the spectrum by a power law function representing a superposition of the white and coloured noise. The green and red solid lines indicate the statistical significance levels of 1-σ (68%) and 2-σ (95%), estimated as described in Sec. 3, step 8. The vertical blue dashed line indicates the oscillation period equal to 0.4 of the total analysed signal length. All the EMD-revealed intrinsic modes with mean periods longer than what could be attributed to the low-frequency trend $T(t)$ in this work. Bottom right: The EMD spectrum (dependence between the EMD-revealed modal energies and mean periods) of the original flare section of interest with the exponential trend $T_{\exp}(t)$ subtracted, see steps 5 and 6 in Sec. 3. The blue solid line shows the expected behaviour of a power-law distributed noise with parameters estimated from the Fourier analysis. The red solid lines show the confidence levels of 95% estimated as described in Sec. 3, step 10. The error bars for the values of the EMD-revealed mean modal periods are estimated as the half-level-width of the global wavelet spectra calculated for each of the intrinsic modes and best-fitted by the Gaussian function.

The analysis of QPP signals that we carried out in this work represents a synergy of the methods used by Broomhall et al. (2019): (i) Fourier transform with detrending by smoothing and not taking the background coloured noise into account, (ii) a Fourier transform without detrending and accounting for the background coloured noise, and (iii) a method of empirical mode decomposition (EMD) with a self-consistent detrending and assessment of the statistical significance of the revealed intrinsic oscillatory modes in comparison with the background coloured noise. More specifically, for each of the identified flare events,
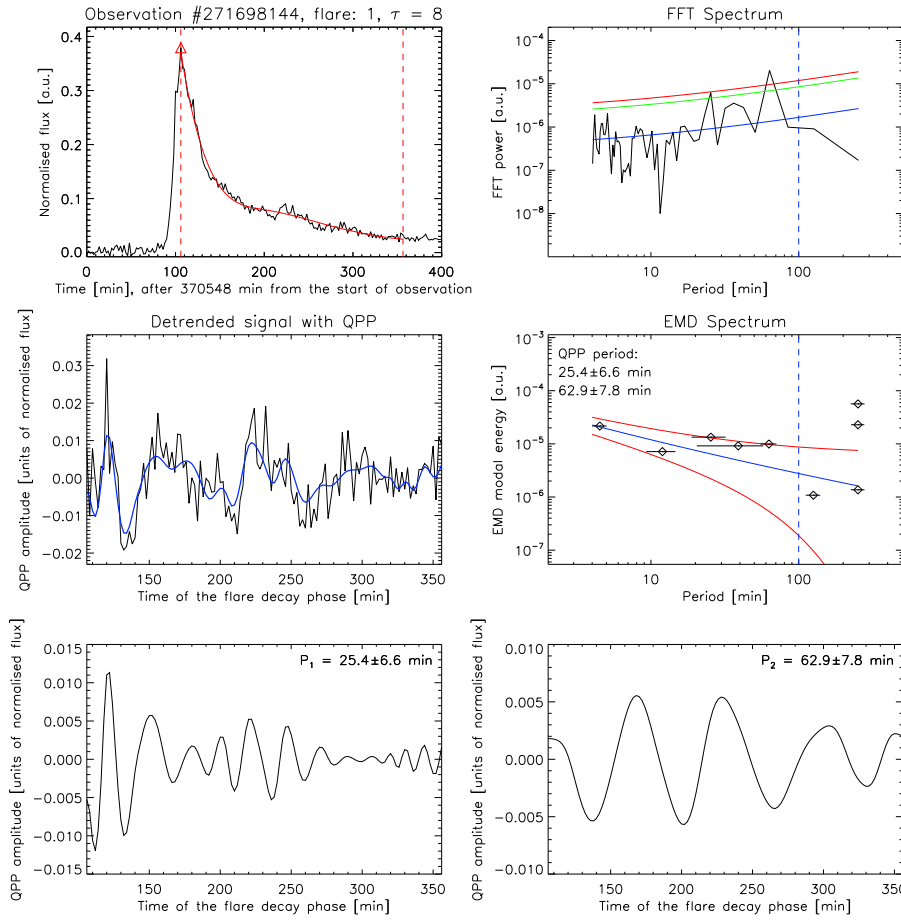
Figure 4. A two-modal QPP event. The layout and notations of the top and middle panels are identical to those shown in Fig. 3. The two bottom panels show the individual EMD-revealed modes of this two-modal QPP event.

1. We focus on the decay phase of the flare, for the beginning of which we use the time of the flare peak (highest value in the flare light curve), t_{peak}; and the above-mentioned $t_{\mathrm{dec}} = 500\,\mathrm{min}$ for its duration.

2. As a rough estimate of the flare e-folding time $t_{1/e}$, we best-fit the decay phase of the flare with an exponential function.

3. To account for the effects of flare trimming on the detection of QPPs (see Sec. 5.3 in Broomhall et al. , 2019), we vary the length of the signal of interest as $[t_{\mathrm{peak}},\ t_{\mathrm{peak}} + \tau t_{1/e}]$, where τ is an integer number varying from 2 to 10 in this work.

4. From the resulting flare sections (i.e. $[t_{\mathrm{peak}},\ t_{\mathrm{peak}}+2t_{1/e}]$, $[t_{\mathrm{peak}},\ t_{\mathrm{peak}}+3t_{1/e}]$, etc.), we select only those in which the number of observational data points is greater than 30. Fewer data points would not allow for a meaningful Fourier or EMD analysis of periodicities.

5. For each of those selected flare sections $F_0(t)$, we subtract the exponential fit $T_{\text{exp}}(t)$ obtained at step 2, as a rough approximation of the flare trend. This gives $F_1(t) \equiv F_0(t) - T_{\text{exp}}(t)$. This allows us to mitigate the discontinuity between the start and end points in $F_0(t)$, which is crucial for the Fourier and EMD techniques.

6. We apply the EMD method to $F_1(t)$. From all the EMD-revealed intrinsic modes, we combine all modes with characteristic time scales longer than 0.4 of the total signal length (so that the number of oscillation cycles in each of those modes is less than 2.5) in a slowly varying trend $T_{\text{emd}}(t)$ of $F_1(t)$.

7. We define the total trend of the original flare signal $F_0(t)$ as $T(t) \equiv T_{\text{exp}}(t) + T_{\text{emd}}(t)$ (see the red solid lines in the top left panel of Figs. 3-4), and subtract $T(t)$ from $F_0(t)$ to obtain the detrended signal $F(t)$.

8. We apply the Fourier analysis to $F(t)$ (see the top right panels in Figs. 3-4) and assess the significance of the Fourier peaks and obtain parameters of the background noise (i.e. its power law index also known as the noise "colour", and energies of the white and coloured components), adapting the methods from Vaughan (2005) and Pugh et al. (2017). We note here that due to the intrinsic non-stationary properties of QPP (i.e. short lifetime, modulation of the oscillation amplitude and/or period) their oscillation energy often gets re-distributed across a number of Fourier harmonics, thus lowering the statistical significance of QPP in the Fourier analysis (see e.g. Nakariakov et al. , 2019, for a recent review of this topic). Hence, in this work we set two significance levels of 1-σ (i.e. 68% confidence) and 2-σ (i.e. 95% confidence) in the Fourier spectra.

9. From this stage onwards, we proceed only with those signals which have the Fourier peaks with significance of at least 1-σ.

10. For those signals, we assess the statistical significance of the EMD modes revealed at step 6, following Kolotkov et al. (2016) and using the parameters of noise obtained from the Fourier analysis at step 8. The corresponding EMD spectra (i.e. the dependence between the EMD-revealed modal energies and mean periods) with the 95% confidence levels are shown in the bottom right panels of Figs. 3-4.

11. We consider a QPP event is positively detected in this work if it has at least 1-σ (68%) significance in the Fourier analysis and 2-σ (95%) significance in the EMD analysis.

The application of this scheme allowed us to reveal eleven QPP events (see Figs. 3-4 and Figs. 9-11) with mean periods ranging from $10.2 \pm 1.4\,\text{min}$ to $71.9 \pm 13.0\,\text{min}$ (see Table 3), including one QPP signal with a strong drift in the oscillation period (see Fig. 3) and one two-modal QPP signal (see Fig. 4). In the QPP event shown in Fig. 3, the instantaneous oscillation period is clearly seen to decrease with time from about 40 min to 20 min, unless the QPP oscillation amplitude becomes comparable to the amplitude fluctuations caused by noise. Because of such strong non-stationarity, the Fourier power of this oscillation is seen to be spread between 20 min and 40 min, that resulted in overall lowering the height of the corresponding Fourier peak below 95% significance level. In contrast, in the EMD method the basis for decomposition is not prescribed a

priori but is derived directly from the data by iterative sifting its local time scales (Huang et al. , 1998). This makes the EMD method more suitable for capturing the non-stationary oscillatory processes in general, and QPP in Solar and stellar flares with strong period drifts in particular, see e.g. Sec. 5.4 in Broomhall et al. (2019) and Sec. 3.3 and 4.4 in Kupriyanova et al. (2020), and references therein.

In the example shown in Fig. 3, the application of EMD allowed the retaining of the energy of a non-stationary oscillatory process seen in the detrended observational signal in a single intrinsic mode (i.e. not distributed over a number of modes or harmonics), that resulted in the statistical significance of this mode above 95% in the EMD spectrum. In the two-modal QPP event (Fig. 4), both modes are seen to have rather stable periods with mean values of 25.4 ± 6.6 min and 62.9 ± 7.8 min, and the statistical significance about or higher than 95% in both the Fourier and EMD approaches. Although the periods of these two modes are longer than a multi-mode flare seen in a pre main sequence M3 star identified in NGTS data (Jackman et al. , 2019), the ratio of the short to long periods are consistent to within a factor ~ 2.

By making certain assumptions concerning the nature of the physical mechanism producing the flares, various studies including those of Mathioudakis et al. (2006) and Jackman et al. (2019) were able to estimate the loop length of the flares where the QPPs originate. To do this, we must first estimate the strength of the magnetic field in the M dwarfs.

Table 3. For those stars showing QPPs we show: the flare energy; the QPP period; the duration of the flare based on the flux returning close to the pre-flare flux; the duration of the flare based on the e-folding time; the loop length assuming the QPP-driving mechanism is due to compressive standing slow magneto-acoustic oscillations, l_{slow}; the loop length via long-wavelength kink oscillations, l_{kink}; the loop length based on the predictions of the coronal magnetic field strength and loop length from Namekata et al. (2017), l_{Nam} (and Fig. 6); l_{slow} compared to the star's radius; the estimated magnetic field of the starspot, B_{spot} and the coronal magnetic field, B_{cor}. For the first QPP event in TIC 271698144 the loop lengths are derived for the longer period QPP.

TIC	Energy Flare (erg)	Period QPP (min)	Dur. (min)	E-fold (min)	l_{slow} (Mm)	l_{kink} (Mm)	l_{Nam} (Mm)	l/R_*	B_{spot} (G)	B_{cor} (G)
1403938	6.0e35	21.5	85	21.2	440	640	580	1.69	2.5k	250
1403938	1.0e34	36.6	145	16.1	750	1000	160	2.87	2.5k	230
233547261	7.5e35	25.8	200	25.2	530	740	730	1.93	2.0k	240
279494336	6.1e35	39.8	120	31.3	810	950	760	2.85	4.0k	200
353898013	8.2e34	19.8	78	20.2	400	400	330	1.76	1.6k	170
455825451	1.1e34	71.9	289	11.9	1470	1380	230	5.68	1.4k	160
271698144	3.4e35	25.4/62.9	250	19.5	1810	1660	570	1.74	3.2k	240
271698144	4.0e34	10.2	60	39.0	210	120	490	0.69	3.2k	100
393804343	1.6e34	13.6	78	16.6	280	230	280	0.95	2.0k	140
393804343	4.3e35	19.7	116	19.8	400	580	600	1.37	2.0k	245
393804343	1.3e34	18.5	140	32.1	380	200	350	1.29	2.0k	90

4. Magnetic Field strengths

Determining the field strength (or upper limit) of any star can be achieved, in principal, using spectropolarimetric data, but this requires considerable telescope time and is restricted to relatively bright stars, e.g. Reiners (2012). However, there are other indirect means to estimate the magnetic field strength of a star provided it shows evidence of rotational modulation. To estimate the magnetic field strength of the stars showing QPPs we begin by using the formula of Maehara et al. (2012) & Notsu et al (2019) to determine the area of spot coverage:

$$\Delta F_{\mathrm{rot}}/F \sim \left[1 - \left(\frac{T_{\mathrm{spot}}}{T_{\mathrm{star}}}\right)\right]^4 \frac{A_{\mathrm{spot}}}{A_{\mathrm{star}}} \tag{1}$$

where $\Delta \mathrm{F_{rot}}/\mathrm{F}$ is the amplitude of the rotational modulation, $\mathrm{T_{spot}}$ and $\mathrm{T_{star}}$ are the spot and stellar effective temperature respectively, $\mathrm{A_{spot}}$ is the area of the star covered by the spot(s) and $\mathrm{A_{star}}$ is the area of the star. To determine the difference between the starspot and the mean photospheric temperature, we use the formula of Notsu et al (2019):

$$T_{\mathrm{star}} - T_{\mathrm{spot}} = 3.58 \times 10^{-5}T_{\mathrm{star}}^2 + 0.249T_{\mathrm{star}} - 808 \tag{2}$$

where we take the effective temperature of the star (T_{star}) from the TIC v8.0 catalogue (Stassun et al. , 2019). The magnetic field strength can then be estimated using the relationship derived by Shibata (2013):

$$E_{\mathrm{flaremax}} = 7 \times 10^{32}\mathrm{erg} \left(\frac{f}{0.1}\right) \left(\frac{B}{10^3}\right)^2 \left(\frac{A_{\mathrm{spot}}/2\pi R^2}{0.001}\right)^{3/2} \tag{3}$$

where E_{flaremax} is the maximum bolometric energy of the flare we detect in that stars light-curve, f is the fraction of the magnetic energy that can be released as flare energy (which we fix at 0.1 as done by Shibata (2013)) and A_{spot} is the area of the spot (taken from Equation 1 above).

Using the equations above we can determine the relationship between the relative size of the starspot and the maximum energy of the flare which we show in Fig. 5. Using equation 3 we can derive the magnetic field of the starspot as a function of area and energy and find $B \sim$1–4 kG. These field strengths are consistent with the magnetic field of starspots in M dwarf stars, e.g. see Morin et al. (2008).

5. Loop lengths

Roberts et al. (1984) outlined how the QPPs seen in Solar flares could be used to determine the loop length of Solar coronal loops and the physical conditions in
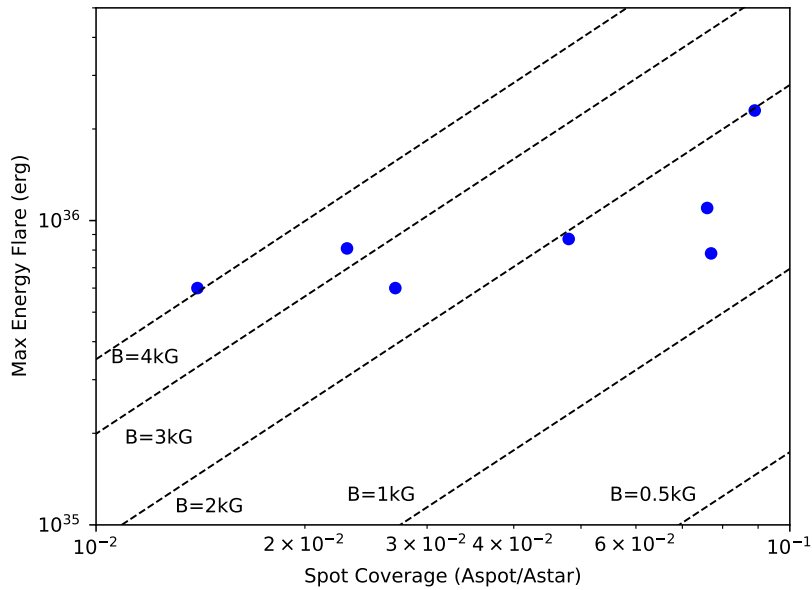
Figure 5. The relationship of spot coverage and the bolometric energy of the most energetic flare from that star. We show the predicted relationship for different magnetic field strengths from equation 3 and Notsu et al (2019).

their immediate environment. The same principles have been used to determine properties of stellar flares using observations of QPPs. Mathioudakis et al. (2006) approximate the formula for the period and loop length to:

$$\text{Period(sec)} = \frac{l_{\text{slow}} \ (\text{Mm})}{7.6 \times 10^{-2} N \sqrt{T(\text{MK})}} \qquad (4)$$

where l_{slow} is the loop length in Mm, N is the node of oscillation (N=1 for the fundamental, N=2 for the first harmonic) and T is the average temperature of the corona along the flare loop which Mathioudakis et al. (2006) take to be 20 MK. The above equation assumes that the QPP-driving mechanism is due to compressive standing slow magnetoacoustic oscillations in coronal loops where the oscillation period is prescribed by the loop length and the sound speed (i.e. square root of temperature).

Assuming N=1, we show the derived loop lengths in Table 3 which are in the range ~200–1800 Mm (they are twice these values if N=2). Taking the radius of each star from the TIC (Stassun et al. , 2019), we find that the loop lengths are typically of the same extent (or greater) as the stellar radius. This is consistent with a study of 44 stars with F-M spectral type which showed that the loops with the largest length to stellar radius ratio ($\sim 2R_*$) originated on M dwarfs (Mullan et al. , 2006), with the shortest loops being comparable to that estimated for the flare reported in Jackman et al. (2019).
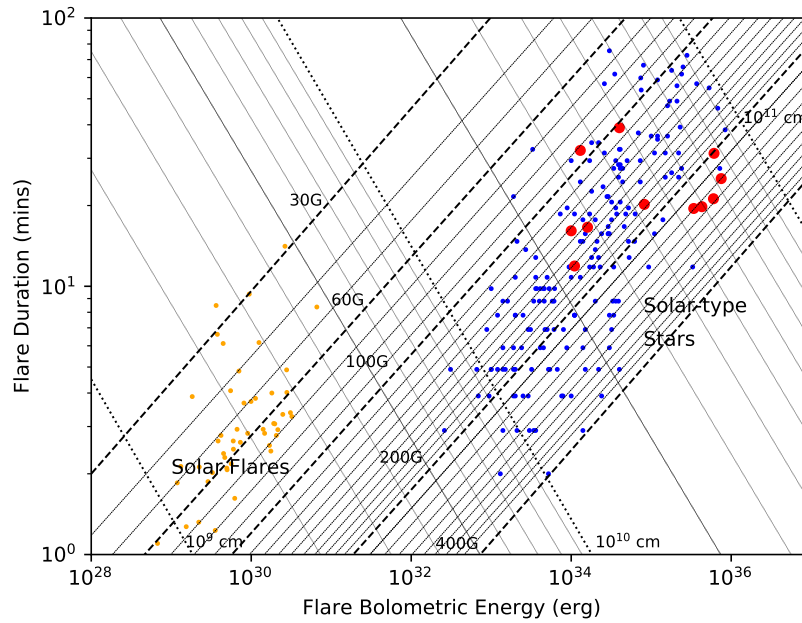
Figure 6. This figure is based on Fig 9 of Namekata et al. (2017) which incorporate work from Maehara et al. (2015). Solar data is shown as orange dots whilst blue dots show super-flares from Solar type stars using *Kepler* data with 1 min cadence. The large red dots are the sources shown in this paper where the energies and duration are derived from *TESS* data. We can use the relationships derived for different magnetic field strength and loop length to estimate these quantities for the stars presented in this paper.

An alternative way of deriving the loop length is via the scaling laws used by Namekata et al. (2017). Taking the flare duration and energy of those flares as outlined in Table 3, we place them in context by adding them to Fig. 9 of Namekata et al. (2017) which shows the energy and duration of Solar flares and Solar-like stars. Our sample of low mass stars are comparable with the more energetic flares from Solar-like stars. We can estimate the loop lengths of the flares in our sample by comparing their location in Fig. 6 with the theoretical relationships for coronal magnetic strength and loop length which were taken from Namekata et al. (2017). Given the uncertainties in the assumptions, the resulting loop lengths are similar to those estimated assuming they are driven by slow magneto-acoustic oscillations. However, no matter which wave mode we use, these loop lengths estimates clearly imply very large active regions covering a significant factor of the stellar surface.

However, alternative QPP-driving options are possible, e.g. fast magnetoacoustic waves which include the *kink oscillations* of coronal loops situated in, or nearby, the flaring active region (Nakariakov et al., 2006). The period of standing kink oscillations is prescribed by the loop length and the Alfvén speed inside the loop (Nakariakov & Kolotkov, 2020). Here we have two unknowns, the loop length and the Alfvén speed. In §4 we estimated a photospheric magnetic field typically in the range ∼1–4 kG. There are obvious uncertainties in predicting

the coronal magnetic field strength from a photospheric field strength (the uncertainty in the height of the loop above the photosphere and the magnetic field configuration) but a reduction of a factor of 10 is reasonable. This yields coronal magnetic field strengths roughly between $\sim$100-300 G (see Table 3) which are in excellent agreement with those derived from Fig. 6. We can use the equation

$$\text{Period} = \sqrt{2} l_{\text{kink}} / C_{\text{Alfvén}} \qquad (5)$$

where l_{kink} is the loop length and $C_{\text{Alfvén}}$ the Alfvén speed based on the derived magnetic field strength, assuming the fundamental (global) harmonic (see Eq. 9 of Nakariakov & Kolotkov (2020)) and a density $\rho_o = 1 \times 10^{-9}$ kg m^{-3} which implies an electron number density, $N_e \sim 1 \times 10^{12}$ cm^{-3} (Monsignori Fossi et al. (1996) found that in the corona of active M dwarfs, $N_e > 1 \times 10^{12}$ cm^{-3} during activity and $N_e \sim 1.5 \times 10^{13}$ cm^{-3} during flares). The derived loop lengths (Table 3) are in good agreement with the lengths derived via the compressive standing slow mode. The sound speed C_s is about the Alfvén speed $C_{\text{Alfvén}}$, i.e. the plasma parameter $\beta = 2C_s^2/(\gamma C_{\text{Alfvén}}^2)$ is around unity. In Solar flares, such high values of β have been observed, e.g. high energy X-class flares require high temperatures and that both the plasma β and volume filling factor cannot be much less than unity in the super-hot region, see Caspi et al. (2014).

We now comment briefly on the parameters for flare energy, duration, loop lengths and magnetic field reported in Table 5. Given the loop lengths are directly linked to the period of the QPP (Eq. 4) there is a clear correlation between these parameters and also period and duration: long duration flares can have long period QPPs whilst short duration flares cannot. Similarly, the correlation between magnetic field strength and duration of the flare comes from the scaling relations of Namekata et al. (2017). Perhaps surprisingly we find no correlation between the flare energy and flare duration.

6. Flare rates and the effects on potential Exoplanets

We now return to the overall flare rates of the seven stars for which we have identified QPPs. We show these rates in Fig. 7 as a cumulative flare frequency distribution (FFD). The seven stars show flares with bolometric energies $> 10^{35}$ erg occurring at a rate of 1 per $\sim$10–100 days: these are higher rates than the average rates for M3V-M4V stars (Howard et al. , 2019).

We do not examine the physical mechanism which enable these stars to produce high energy flares at such high rates. Rather, we examine what effect these flares may have on the atmosphere of any orbiting exoplanet. Over the past 25 years nearly 4,300 exoplanets have been discovered with thousands more awaiting confirmation. As a result, we now know the majority of main sequence stars are likely to host planetary systems. Furthermore, the study of stellar activity (including flares) on these host stars has become particularly prominent in exoplanet research. This is due to the impact on the exoplanet atmosphere
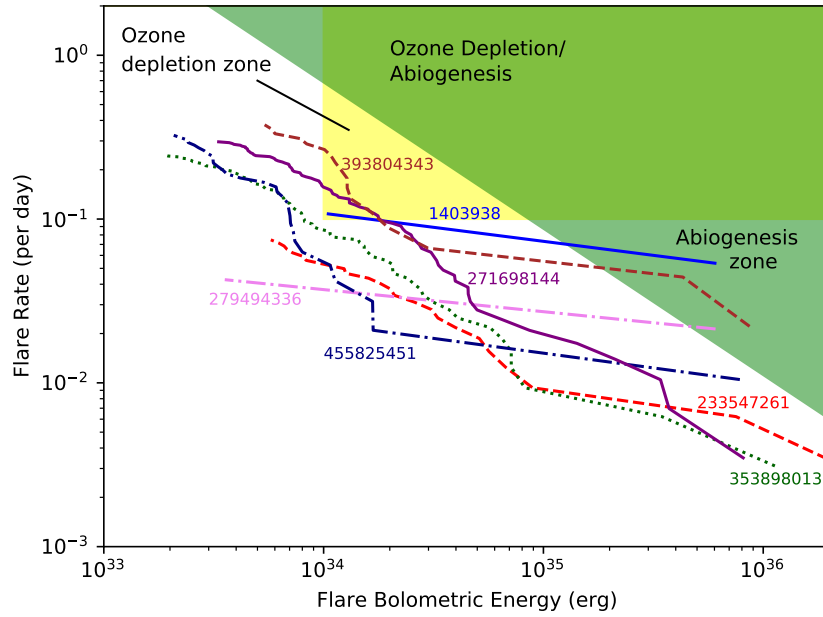
Figure 7. The Flare Frequency Distribution (FFD) for flares of given energy for all seven stars in our sample which show QPPs. The Solar FFD, during both maximum and minimum, have maximum energies which are lower than the minimum energy shown here. We show the regions where terrestrial exoplanets in the habitable zone will have ozone in their atmosphere depleted and also lie in the abiogenesis zone, which were taken from Figure 11 of Günther et al. (2020) which was adapted from work of Tilley et al. (2019) and Rimmer et al. (2018).

and the existence for life along with the potential of exoplanet signals being masked by stellar variability.

It is widely known that for life to exist, the planet must lie within the habitable zone (HZ) of the star. This is a planets distance from the star where liquid water is likely to pool on the surface. However, this is not the only requirement for life. In Rimmer et al. (2018), they use experimental chemistry along with stellar physics to determine how much energy would be needed for abiogenesis (natural process where life arises from non-living matter) to occur. They compute this for a sample of low mass stars from Davenport (2016), concluding that ∼20% of early M dwarfs are active enough for any host planets to be in the abiogenesis zone. The abiogenesis zone indicates where the stellar UV flux is large enough to result in a 50% increase of the photo-chemical product (i.e. those products which are present in the nucleotide synthesis pathway, see Fig. 1 of Rimmer et al. (2018) for more details).

Furthermore, there is an ozone depletion region where flare rates can cause ozone loss for a planet orbiting in the HZ around an M dwarf. Understanding the effects of flaring activity on an exoplanet atmosphere is essential in predicting whether there is life on the surface of the planet. The exoplanet could well be in the HZ, however, it may also be bombarded by electromagnetic and particle radiation from the star. Tilley et al. (2019) looked into this in more detail using

models to investigate the effects of repeated flaring on the photochemistry and surface UV of an Earth-like planet (unprotected by a magnetic field) orbiting an M dwarf. Overall, they found Coronal Mass Ejections (CMEs), which are commonly associated with flares possessing energies $> 10^{34}$ erg, were the primary factor in ozone depletion, at a rate greater than once every ten days. The ozone is particularly important for the existence of surface life as this thin layer is responsible for absorbing almost all of the harmful UV radiation.

We have taken the location of the Ozone depletion and Abiogenesis zones from Fig. 11 of Günther et al. (2020), who have determined the abiogenesis zones for FGKM stars and for flare energies in the U and the bolometric energies (as we have derived). Specifically we use the regions determined for M0-M4 stars. As can be seen from Fig. 7, three stars have FFDs which overlap with the ozone depletion zone. This means any potential exoplanets orbiting these stars could have their ozone layer destroyed by the constant flaring activity. The frequency of this high energy flaring means the atmosphere of an exoplanet is unlikely to have time to recover, being destroyed over a prolonged period of time assuming the absence of a magnetic field environment. Although, whether a magnetic field adds sufficient protection remains unanswered. For example, magnetised Earth has a relatively thick atmosphere whereas Mars, which is unmagnetised, does not. However, on the other hand, Venus which is also unmagnetised has a relatively thick and dense atmosphere. Regardless of this, the UV radiation exposed to any potential exoplanets would make it difficult for surface life to exist. This does not rule out the existence of life altogether as there could be some present below the ocean surfaces.

There are three stars in the sample which have FFDs which extend to the abiogenesis zone: TIC 393804343, TIC 1403938 and TIC 279494336. For these stars this is significant as it indicates the high energy flares of $\sim 5 \times 10^{35}$ erg at a frequency of one every $\sim$20–50 days, is an important factor in the potential for life on any orbiting exoplanets. However, there is a fine line where too many high energy flares at a high frequency can cause ozone depletion. We see an example of this in TIC 1403928 and TIC 393804343 which lie in both the ozone and abogenesis zones. The question for this particular star is whether any orbiting planets atmosphere will have enough time to recover, allowing for abiogenesis and surface life to potentially exist. The remaining stars do not lie in either the abiogenesis or ozone depletion zones, although they do show high energy flares but at rates slightly lower than required to be in the abiogenesis zone. As a result, the ozone layer on any orbiting planets will likely remain intact and the UV flux is not high enough to sustain prebiotic chemistry. This does not mean there is no potential for any surface life on orbiting planets, just that it is less likely to manifest without the natural environment needed.

Most M dwarfs have not been observed in EUV/UV. However, Melbourne et al. (2020) derived a relationship between Ca II H&K and Hα with various strong FUV/NUV lines. The derived scaling relations may be sufficient for photochemical modelling needs, but not atmospheric escape modelling, although an accurate estimate of the Ly α flux should account for $\sim$75% of the FUV in the quiescent state and $\sim$50% during a flare (Diamond-Lowe et al. , 2021). Unfortunately, we do not yet have the Ca II H&K or Hα flux for these objects.

In Fig. 8, we show a schematic plot of how far the coronal loops extend out from the stellar surface in relation to the HZ. In determining this, we assume the loops are semi-circular arcs which are equal to the loop length. As a result, the radius of the arc is then the distance at which the loop extends out from the stellar surface and can be calculated as $R_{\mathrm{loop}} = l/\pi$. It is important to note that this yields a conservative estimate on the radius of the loop, as most loops are not perfect semi-circular arcs but appear more elliptical in shape. However, for the purposes of this paper assuming a semi-circular arc is acceptable. For stars which possessed more than one QPP event in Table 3 the QPP with the largest loop length was used. The HZ boundaries were calculated using Kopparapu et al. (2013, 2014) taking the effective stellar temperature, T_{eff}, and luminosity, L, from Table 1.

It is important to note that none of the targets in this sample have any known exoplanets according to the NASA Exoplanet Archive[4]. This does not mean there are none present at all, just that none have been detected around these stars as of yet. In fact, the occurrence rate for exoplanets orbiting mid-M dwarfs is on average 1.2 planets per star (Hardegree-Ullman et al. , 2019) so, each of these targets is expected to have at least one orbiting exoplanet.

7. Discussion

The promise of finding QPPs in *TESS* observations of low mass dwarf stars was demonstrated in observations of Proxima Centauri which showed oscillations on a period of several hours in the decay phase of two flares (Vida et al. , 2019). The work presented here shows the scope for identifying and analysing QPPs from a larger sample of low mass stars using *TESS* data.

Of the 178 M dwarfs which we detected at least one flare with an amplitude corresponding to >0.5 mag and duration longer than 1 hr, we found 11 flares from 7 stars which showed QPPs. Therefore only 4% of the stars showed flares with QPPs.

However, of those stars which *did* show QPPs, we find a very diverse rate for the fraction of flares which showed QPPs. For instance, QPPs were detected in both of the two flares seen in TIC 1403938. In contrast, for TIC 353898013 only 1 out of 79 flares showed a QPP. However, those stars with relatively high fractional rates also has the shortest duration of observations so this may simply be an observational bias.

In several instances, the flare showing QPPs was not the most energetic event of that star, which raises a question of the excitation of waves in stellar atmospheres by powerful flares, to be addressed in follow up work. However, we note that 11 QPP events detected in this work constitute 7% of the total number of flares examined (150), which is a factor of two greater than the statistics of stellar QPPs previously reported (Balona et al. , 2015; Pugh et al. , 2016), and coincide with the fraction of Solar C-class flares which show QPPs (Hayes et al. , 2020). We now briefly discuss the robustness of the loop lengths we derive, the effect of QPPs on any orbiting exoplanets and look ahead to future observations.
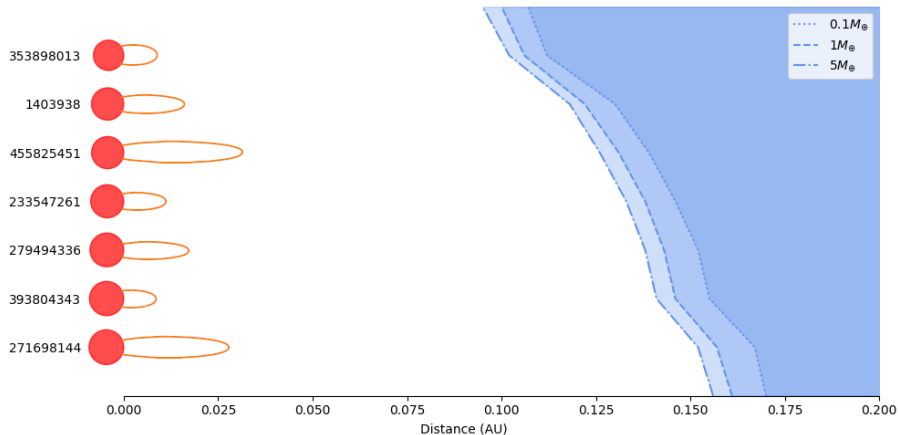
---

[4]https://exoplanetarchive.ipac.caltech.edu/

Figure 8. A schematic diagram showing how far the coronal loops (compressive standing slow mode) extend out from the stellar surface, relative to where the HZ lies from the star. The inner HZ boundary is shown for 0.1 (dotted), 1 (dashed) and $5M_\oplus$ (dashed-dot) and the outer boundary lies between 0.2 and 0.3 AU (not shown in the diagram). These HZ boundaries were calculated using Kopparapu et al. (2013, 2014) and loop lengths (l_{slow}) were taken from Table 3.

7.1. Loop Lengths and Scaling Laws

As outlined in §1, there are over a dozen possible QPP mechanisms. However since, we are dealing with oscillations with periods of tens of minutes, most of these are not possible. In each of the QPP mechanisms discussed in §5 we have made a number of assumptions. For example, with the slow mode waves we assume a coronal flare temperature of 20 MK; using say 10 MK instead will decrease the estimate by $\sim$30% ($\propto \sqrt{T}$). For the kink waves, there is some uncertainty regarding the plasma density. In flare conditions, the density can be high; e.g. an order of magnitude increase will decrease the Alfvén velocity and the loop length by a factor of three. Considering the various approximations and assumptions used in all three loop length calculations, the derived lengths can only be considered good to an accuracy of a factor of two. Nevertheless, the derived lengths are all comparable with the star's radius and as shown in the illustration in Fig. 8, these loops extend high into the star's corona, thus providing intense UV radiation into a planet's HZ.

Whilst we considered the kink and slow magnetoacoustic modes of a coronal loop as the most common and straight forward mechanisms for QPPs, a more detailed discussion of this question is beyond the scope of this work. Indeed, the problem of the association of the observed QPP signals to the wave and oscillatory phenomena in solar and stellar atmospheres has been actively debated for at least the last fifteen years and still remains an open question (Zimovets et al. , 2021). To address the question of which mechanism drives the QPP events and to gain a better understanding of the physical mechanism producing white light flares will require many more QPPs to be detected and studied.

7.2. Possible Effects of QPPs on Orbiting Exoplanets?

Since the launch of *TESS*, the discovery of planets orbiting M dwarf host stars has rapidly increased. These low mass stars spend billions of years on the main sequence due to their cooler temperature. As a result, this would provide enough time for life to flourish on the surface of orbiting exoplanets making the study of exoplanet habitability of particular importance. In section 6, we discussed the flare energy and rate of our M dwarf sample and whether any of the stars possess the conditions needed for abiogenesis or ozone depletion. However, we did not discuss the effects of QPPs on the atmosphere of an exoplanet. Hayes et al. (2017) investigated the effects of Solar flare X-ray QPPs on the Earth's atmosphere. They found pulsations within the lower ionosphere of the Earth matched those of observed Solar QPPs. This QPP-driven periodic modulation of the conditions in Earth's lower ionospheric (e.g. the electron number density) could result in phenomena such as acoustic gravity waves (e.g. Nina & Čadež (2013)), and disruptions in high-frequency radio wave propagation (e.g. Frissell et al. (2019)), implying a similar response could be found in exoplanet atmospheres.

If a planet was orbiting close enough to the host star then magnetospheric interactions could be possible. This is when the host star and close-in planets magnetic fields interact causing Star Planet Interactions (SPIs) in the form of increased chromospheric emission and possibly flaring (see, Ip et al. (2004); Cohen et al. (2010); Strugarek et al. (2014). In our stars, we have coronal loops which extend out to between 0.008 to 0.03 AU (see, Fig. 8). None of the stars in our sample have known exoplanets, however, there have been exoplanets detected around other low mass stars within this range (for example the TRAPPIST-1 system Gillon et al. , 2017). TRAPPIST-1 has seven planets orbiting an M8 dwarf star with semi major axis between 0.01 and 0.06 AU. This means that at least four of the planets are orbiting the star within the range of the coronal loops we observe on our sample. Therefore, it is possible to have planets orbiting within the loops, outwith the HZ, causing SPIs with the host star. The effects this would have on the planet would make it unlikely for any surface life to exist due to an increase in flare activity resulting in an onslaught of harmful radiation.

8. Future Observations & Conclusions

The *TESS* satellite completed its primary mission (covering Cycle 1 and 2) in July 2020 during which it covered the majority of the sky. In each hemisphere, there was an area at each ecliptic pole known as the continuous viewing zone where stars could be observed for a year (some gaps are present due to roughly monthly field re-pointing). During Cycle 1 and 2, around 20,000 stars were observed in 2 min cadence mode with 30 min cadence data being available for all stars through full-frame image data.

The extended mission started in July 2020 by re-observing the southern ecliptic hemisphere. There was, however, a clear difference in the cadence of targets. Around 600 targets will be made available to be observed in 20 sec cadence through the Guest Observer Programme and 15,000 targets will be observable

in 2 min cadence mode. The full-frame images will now be made available with a cadence of 10 min.

Bright low mass dwarfs which have already been shown to be flare active, will be excellent targets to observe in 20 sec cadence mode as it will provide increased time resolution of QPP events. This is especially true for shorter period QPPs which will possess shorter loop lengths. For long duration flares, the full frame data will prove useful in extending the sample of stars showing QPP events.

Stars which have shown QPPs in *TESS* data will be excellent targets to be observed using high cadence ground based imagers such as ULTRACAM. Previous observations made using ULTRACAM have allowed the colour, and hence temperature, of the flare to be determined over the event, which have provided the base material to test competing models which give rise to the QPP events (e.g. Kowalski et al. , 2016). The derived loop sizes from the QPPs is consistent with work by Cohen et al. (2017) who found that at high latitudes the corona and its X-ray emission are dominated by star-size large hot loops. These authors suggested that in rapidly rotating stars, emission from such coronal structures dominates the quiescent saturated X-ray emission.

The work presented here shows the scope for identifying and analysing QPPs from a larger sample of low mass stars. We found 7 stars which show a total of 11 QPP events, one of which is a double mode event. With future TESS 20 sec cadence data, we can expand on this work sampling shorter periods which will allow a better comparison with Solar data. For example, Hayes et al. (2020) analysed 5,519 Solar flares observed in the X-ray, covering X-, M- and C-class events in the past Solar cycle. Looking at periodicities in the 6-300 s timescale the authors found QPPs in 46% of X-class, 29% of M-class, and 7% of C-class flares. The data used here does not allow us to search this period range, but future TESS data will allow us to look for periods down to ~ 60 s and in particular look at events with energy classifications ranging up to X100,000; an energy range not possible for Solar flares.

Using the observed properties of the stars we estimate the length of the loops giving rise to the flares: they are typically of the order of the stellar radius. The observed properties of QPPs are found to be consistent with the interpretation in terms of magnetoacoustic waves potentially present in the atmospheres of the observed stars. However, we could not discriminate between the fast or slow magnetoacoustic modes because they have rather similar observational properties in high-β flaring plasmas. We fully expect other QPPs to be identified in future *TESS* data.

Acknowledgements

References

Airapetian, V. S., et al. 2020, IJAsB, 19, 136

Aller, A., Lillo-Box, J., Jones, D., et al., 2020, A&A, 635, 128

Anfinogentov, S., Nakariakov, V. M., Mathioudakis, M., Van Doorsselaere, T., Kowalski, A. F., 2013, A&A, 773, 156

Astraatmadja, T. L., Bailer-Jones, C. A. L., 2016, ApJ, 832, 137

Balona, L. et al., 2015, MNRAS, 450, 956

Broomhall, A.-M. et al. 2019, ApJS, 244, 44

Caspi, A., Krucker, S., Lin, R.P., 2014, ApJ, 781, 43

Cho, I.-H., Cho, K.-S., Nakariakov, V. M., Kim, S., Kumar, P., 2016, ApJ, 830, 110

Cohen, O., et al. 2010, JGRA, 11510104

Cohen, O., et al. 2017, ApJ 834, 14

Davenport, J. R. A., 2016, Astrophysics Source Code Library, 1608.003

Davenport, J. R. A., et al 2019, ApJ, 871, 241

Doyle, J.G., et al. 2018, MNRAS, 475, 2842

Doyle, L., Ramsay, G., Doyle, L., 2020, MNRAS, 494, 3596

Diamond-Lowe et al, 2021, arXiv2014095119

Frissell, N. A., et al., 2019, SpWea, 17, 118

Gaia Collaboration, Brown, A.G.A., Vallenari, A., et al. 2018a, A&A, 616, A1

Gillon, M., et al. 2017, Nature, 542, 456

Günther, M. N., Zhan, Z., Seager, S., et al., 2020, AJ, 159, 60

Hartman, J. D., Bakos, G. Á., 2016, A&C, 17, 1

Hardegree-Ullman, K. K., Cushing, M. C., Muirhead, P. S., Christiansen, J. L., 2019, AJ, 158, 75

Hayes, L. A., et al., 2017, JGRA, 122, 9841

Hayes, L. A., et al., 2020, ApJ, 895, 50

Hedges, C., Luger, R., Dotson, J., Foreman-Mackey, D., Barentsen, G., 2021, AJ, 161, 95

Huang, N. E., et al., 1998, RSPSA, 454, 903

Howard, W. S., et al., 2019, ApJ, 881, 9

Ip, W.-H., Kopp, A., Hu, J.-H., 2004, ApJ, 602, L53

Jackman, J. A. G., et al., 2019, MNRAS, 482, 5553

Jackman, J. A. G., Shkolnik, E., Parke Loyd, R. O., 2021, MNRAS, 502, 2033

Kolotkov, D. Y., Anfinogentov, S. A., Nakariakov, V. M., 2016, A&A, 592, A153

Kopparapu, R. K., et al., 2013, ApJ, 765, 131

Kopparapu, R. K., et al., 2014, ApJ, 787, 29

Kowalski, A. F., et al., 2016, ApJ, 820, 95

Kupriyanova, E. G., Kolotkov, D., Nakariakov, V., Kaufman, A., 2020, STP, 6a, 3

Lightkurve Collaboration, Cardoso, J. V. d. M., Hedges, C., Gully-Santiago, M., et al., 2018, Astrophysics Source Code Library, 1812.013

Maehara, H., Shibayama, T., Notsu, S., et al. 2012, Natur, 485, 478

Maehara, H., Shibayama, T., Notsu, Y., et al. 2015, EP&S, 67, 59

Mathioudakis, M., Bloomfield, D. S., Jess, D. B., Dhillon, V. S., Marsh, T. R., 2006, A&A, 456, 323

Melbourne, K., et al. 2020, AJ, 160, 269

McLaughlin, J. A., et al., 2018, SSRv, 214, 45

Mitra-Kraev, U., Harra, L. K., Williams, D. R., Kraev, E., 2005, A&A, 436, 1041

Morin et al. 2008, MNRAS, 390, 567

Monsignori Fossi, B. C., Landini, M., Del Zanna, G., Bowyer, S., 1996, ApJ, 466, 427

Mullan, D. J., Mathioudakis, M., Bloomfield, D. S., Christian, D. J., 2006, ApJS, 164, 173

Mursula, K., Usoskin, I. G., Maris, G., 2007, Adv Space Res, 40, 885

Nakariakov, V. M., Foullon, C., Verwichte, E., Young, N. P., 2006, A&A, 452, 343

Nakariakov, V. M., et al., 2019, PPCF, 61a4024

Nakariakov, V. M., Kolotkov, D. Y., 2020, ARA&A, 58, 441

Namekata, K., et al., 2017, ApJ, 851, 91

Nandy, D., Martens, P.C.H., Obridko, V. et al. 2021, Prog Earth Planet Sci 8, 40

Severe Space Weather Events: Understanding Societal and Economic Impacts: A Workshop Report. Washington, DC: The National Academies Press. https://doi.org/10.17226/12507

Nina, A., Čadež, V. M. 2013, GeoR, L40, 4803

Notsu, Y., Maehara, H., Honda, S., et al. 2019, ApJ, 876, 58

Osten, R.A. & Bastian, T.S., 2006, ApJ, 637, 1016

Osten, R.A. & Bastian, T.S., 2008, ApJ, 674, 1078

Pecaut M. J., Mamajek E. E., 2013, ApJS, 208, 9

Pugh, C.E., et al., 2016, MNRAS, 459, 3659

Pugh, C.E., et al., 2017, A&A, 602, A47

Ramsay, G., Doyle, J. G., Doyle, L., 2020, MNRAS, 497, 2320

Rajpaul, V., Aigrain, S., Osborne, M. A., Reece, S., Roberts, S., 2015, MNRAS, 452, 2269

Reale, F. et al., 2018, ApJ, 856, 51

Reiners, A., 2012, Living Reviews Solar Physics, 9, 1

Reinhold, T., et al. 2020, Sci, 368, 518

Ricker G. et al., 2015, JATIS, 1a4003

Rimmer, P. B., et al., 2018, SciA, 4, 3302

Roberts, B., Edwin, P. M., Benz, A. O., 1984, ApJ, 279, 857

Rodono, M., 1974, A&A, 32, 337

Shibata, K., Isobe, H., Hillier, A., et al. 2013, PASJ, 65, 49

Schmitt, J. H. M. M., Ioannidis, P., Robrade, J., Czesla S., Schneider, P. C., 2019, A&A, 628, A79

Skumanich, A., 1986, ApJ, 309, 858

Stassun, K., et al., 2019, AJ, 158, 138

Strugarek, A., Brun, A. S., Matt, S. P., Réville, V., 2014, ApJ, 795, 86

Tilley, M. A., Segura, A., Meadows, V., Hawley, S., Davenport, J., 2019, AsBio, 19, 64

Tu, Z.-L., Yang, M., Zhang, Z. J., Wang, F. Y., 2020, ApJ, 890, 46

Van Doorsselaere, T., Kupriyanova, E. G., Yuan, D., 2016, SoPh, 291, 3143

Vaughan, S., 2005, A&A, 431, 391

Vida, K., Kővári, Z., Pál, A., Oláh, K., Kriskovics, L., 2017, ApJ, 841, 124

Vida, K. et al., 2019, ApJ, 884, 160

Zimovets, I. V., McLaughlin, J. A., Srivastava, A. K., et al. Space Sci Rev, 2021, 217, 66
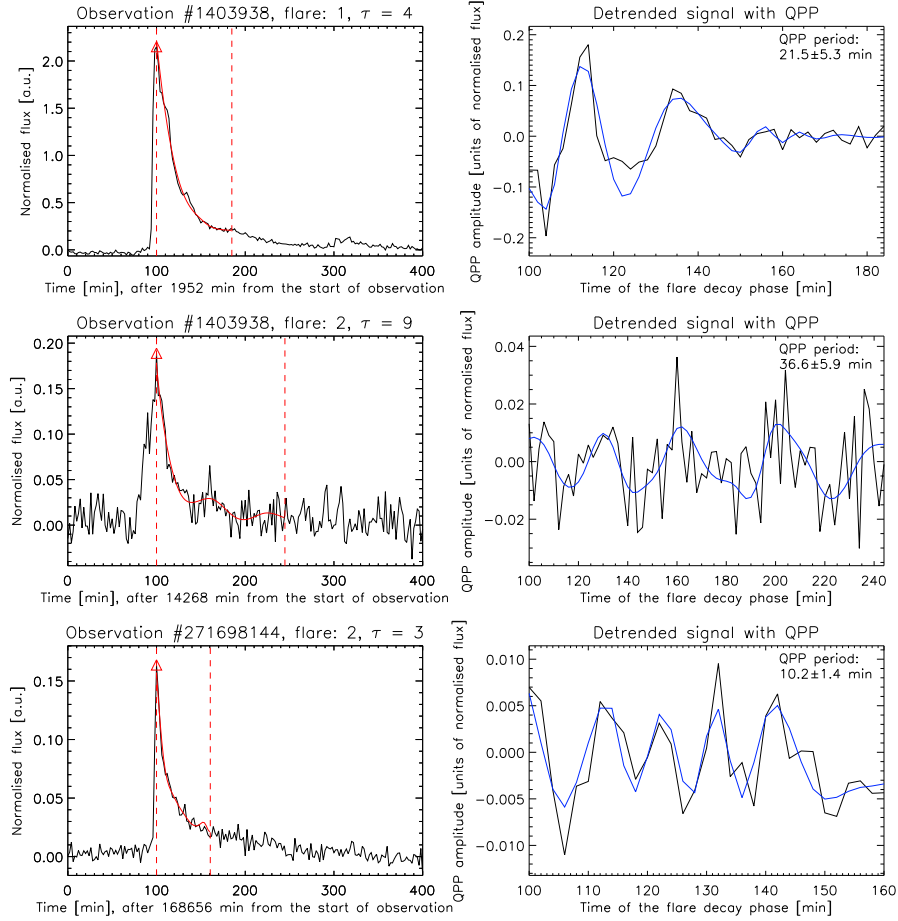
Appendix

A. QPP signals

Figure 9. The QPP signals detected in observations TIC 1403938 and TIC 271698144. See Fig. 3 for details on the figure notations.
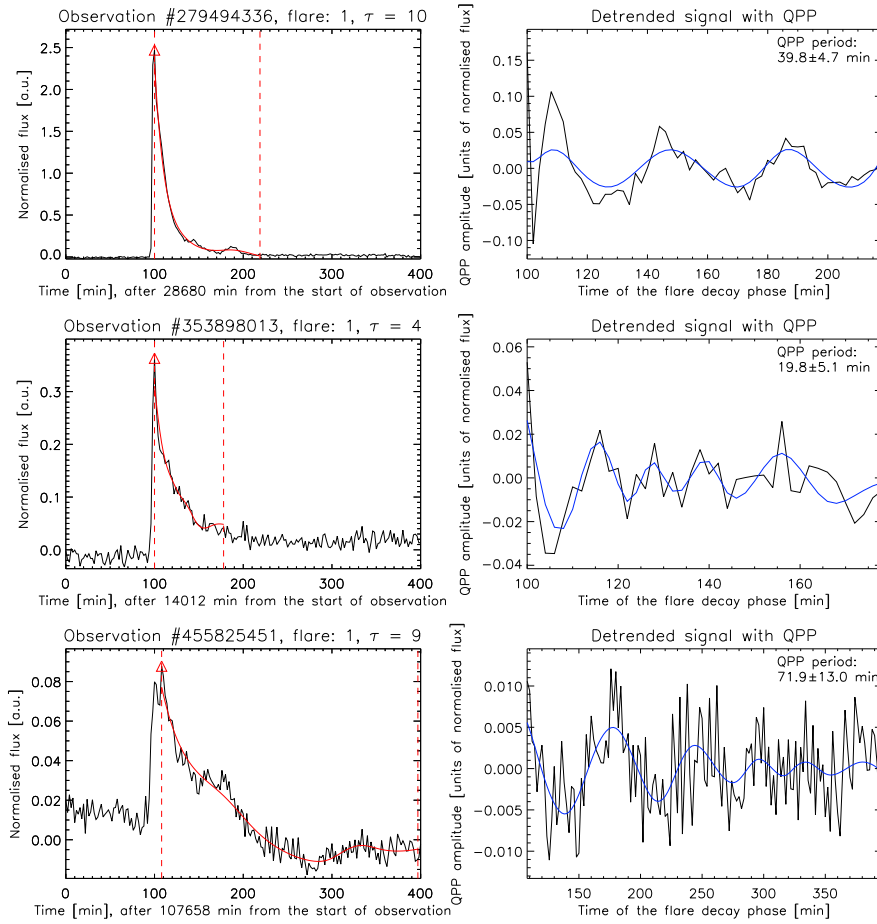
Figure 10. The QPP signals detected in observations TIC 279494336, TIC 353898013, and #455825451. See Fig. 3 for details on the figure notations.

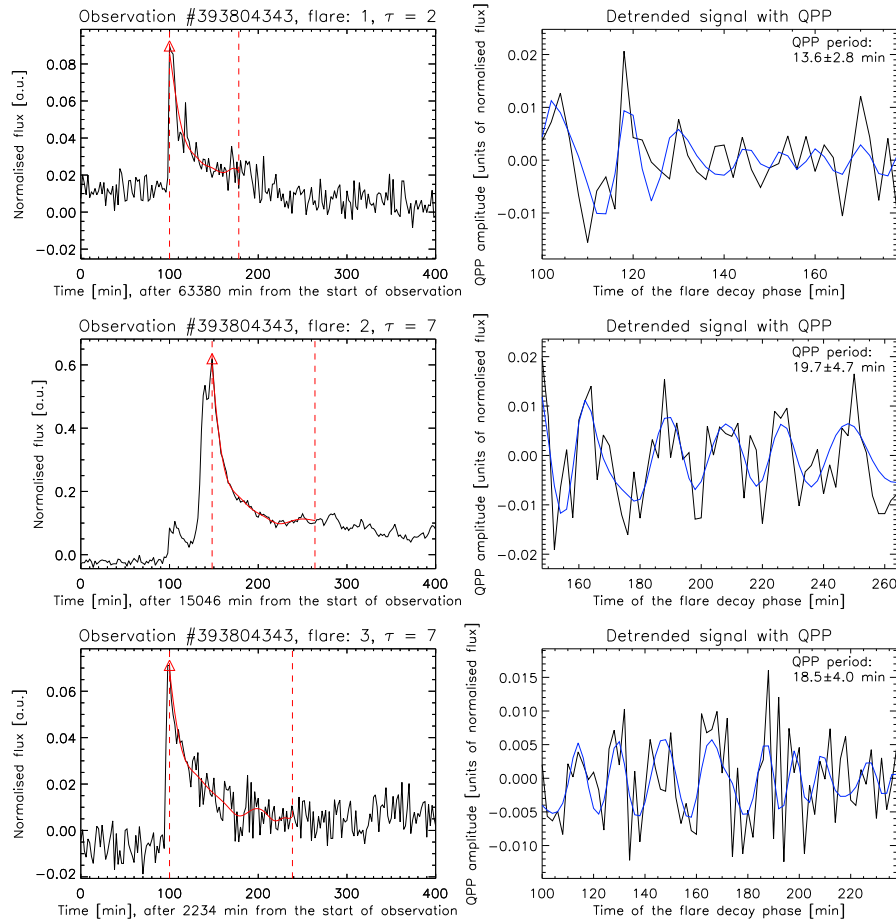**Figure 11.** The QPP signals detected in observation TIC 393804343. See Fig. 3 for details on the figure notations.